

AKARI IRC 2.5–5 μm SPECTROSCOPY OF INFRARED GALAXIES OVER A WIDE LUMINOSITY RANGE

KOHEI ICHIKAWA¹, MASATOSHI IMANISHI², YOSHIHIRO UEDA¹, TAKAO NAKAGAWA³,
 MAI SHIRAHATA^{3,4}, HIDEHIRO KANEDA⁵, AND SHINKI OYABU⁵

¹ Department of Astronomy, Graduate School of Science, Kyoto University, Kitashirakawa-Oiwake cho, Kyoto 606-8502, Japan;
ichikawa@kusastro.kyoto-u.ac.jp

² Subaru Telescope, 650 North A'ohoku Place, Hilo, HI 96720, USA

³ Institute of Space and Astronautical Science (ISAS), Japan Aerospace Exploration Agency, 3-1-1 Yoshinodai, Chuo-ku, Sagami-hara, Kanagawa 252-5210, Japan

⁴ National Institutes of Natural Science, National Astronomical Observatory of Japan (NAOJ) 2-21-1 Osawa, Mitaka, Tokyo 181-8588, Japan

⁵ Graduate School of Science, Nagoya University, Furo-cho, Chikusa-ku, Nagoya, Aichi 464-8602, Japan

Received 2014 January 4; accepted 2014 August 25; published 2014 October 1

ABSTRACT

We present the result of a systematic infrared 2.5–5 μm spectroscopic study of 22 nearby infrared galaxies over a wide infrared luminosity range ($10^{10} L_{\odot} < L_{\text{IR}} < 10^{13} L_{\odot}$) obtained from the *AKARI* Infrared Camera (IRC). The unique band of the *AKARI* IRC spectroscopy enables us to access both the 3.3 μm polycyclic aromatic hydrocarbon (PAH) emission feature from star-forming activity and the continuum of torus-dust emission heated by an active galactic nucleus (AGN). Applying our AGN diagnostics to the *AKARI* spectra, we discover 14 buried AGNs. The large fraction of buried AGNs suggests that AGN activity behind the dust is almost ubiquitous in ultra-/luminous infrared galaxies (U/LIRGs). We also find that both the fraction and energy contribution of buried AGNs increase with infrared luminosity from $10^{10} L_{\odot}$ to $10^{13} L_{\odot}$, including normal infrared galaxies with $L_{\text{IR}} < 10^{11} L_{\odot}$. The energy contribution from AGNs in the total infrared luminosity is only $\sim 7\%$ in LIRGs and $\sim 20\%$ in ULIRGs, suggesting that the majority of the infrared luminosity originates from starburst activity. Using the PAH emission, we investigate the luminosity relation between star formation and AGNs. We find that these infrared galaxies exhibit higher star formation rates than optically selected Seyfert galaxies with the same AGN luminosities, implying that infrared galaxies could be an early evolutionary phase of AGN.

Key words: galaxies: active – galaxies: nuclei – infrared: galaxies

Online-only material: color figures

1. INTRODUCTION

Dust emission gives us crucial information to understand both the history of cosmic star formation in galaxies and that of supermassive black hole (SMBH) growth in galactic centers. Intense star formation produces a great amount of dust, which makes its activity invisible in the ultraviolet band but visible in the infrared band. Similarly, the central engines of active galactic nuclei (AGNs) are surrounded by dusty “tori” (Krolik & Begelman 1986). Since optical and ultraviolet lights are very easily obscured by the torus, the most complete search for AGNs can be made by detecting hard X-rays from the central engine or infrared emission from the heated dust. Utilizing X-ray data of the Chandra Deep Field South, Brightman & Ueda (2012) reported that the fraction of “Compton-thick” AGNs (those with absorption column densities of $N_{\text{H}} > 10^{24} \text{ cm}^{-2}$) increases with redshift from $z = 0$ to $z > 1$. This fact implies that the level of dust obscuration of AGNs may be correlated to the star formation activity, which has a peak at $z \sim 2$ (Hopkins & Beacom 2006). Indeed, Goulding et al. (2012) gathered all available *Spitzer* spectra of local Compton-thick AGNs and found strong starburst (SB) features in their average infrared spectrum, suggesting that SB activity and highly obscured tori are somehow coupled with each other. Ichikawa et al. (2012a) also reported the same trend for buried AGNs with small opening angles of tori (“new type” AGNs; Ueda et al. 2007; Winter et al. 2009; Eguchi et al. 2009, 2011) detected in the *Swift*/BAT survey. Although hard X-rays are useful to search for obscured AGNs (Ricci et al. 2011), extremely heavily buried AGNs with $N_{\text{H}} > 10^{24.5} \text{ cm}^{-2}$ are difficult to detect owing to flux attenuation by repeated Comptonization even at

energies above 10 keV (e.g., Ikeda et al. 2009; Brightman & Nandra 2011).

Candidates of galaxies that host such buried AGNs are infrared galaxies, defined as those having large infrared luminosities (L_{IR}) with $L_{\text{IR}} \geq 10^{10} L_{\odot}$. Among infrared galaxies, those in the range $10^{11} L_{\odot} \leq L_{\text{IR}} < 10^{12} L_{\odot}$ are called luminous infrared galaxies (LIRGs; Sanders & Mirabel 1996), and more luminous ones in the range $10^{12} L_{\odot} \leq L_{\text{IR}} < 10^{13} L_{\odot}$ are called ultraluminous infrared galaxies (ULIRGs; Sanders et al. 1988). Their bolometric luminosities are dominated by the infrared emission, suggesting that very luminous heating sources are surrounded by dust and then the heated dust reemits in the infrared band. The hidden energy sources are believed to be either SBs, AGNs, or both. Disentangling the energy sources of infrared galaxies is crucial to unveil the history of dust-obscured star formation and SMBH growth in the universe (Le Floc’h et al. 2005; Goto et al. 2010; Magnelli et al. 2011; Murphy et al. 2011).

Veilleux et al. (1995, 1999) and Yuan et al. (2010) studied AGN activity in U/LIRGs on the basis of optical observations. They showed that the fraction of AGNs increases with infrared luminosities in the range of $10^{10} L_{\odot} \leq L_{\text{IR}} < 10^{13} L_{\odot}$. One caveat of their optical diagnostics is that one cannot identify buried AGNs embedded in dust tori with very small opening angles where no significant narrow-line regions can be formed. Unlike the AGNs that are optically classified type 2 Seyfert, such buried AGNs are elusive to conventional optical spectroscopy (Maiolino et al. 2003). After the launch of *Spitzer*, the AGN activity in local U/LIRGs was also addressed in the infrared band. Nardini et al. (2008, 2009, 2010) observed ULIRGs with *Spitzer*/IRS 5–8 μm spectroscopy and investigated both the SB and AGN contributions by fitting SB/AGN templates

to the spectra. They found the increasing AGN significance with infrared luminosity, confirming the same trend reported from the optical studies. Alonso-Herrero et al. (2012) observed the 5–38 μm spectra of LIRGs with *Spitzer*. They decomposed the spectra into SB and AGN components using an SB galaxy template and clumpy torus models (Nenkova et al. 2008a, 2008b; Asensio Ramos & Ramos Almeida 2009), which are supported by observations (e.g., Gandhi et al. 2009; Ichikawa et al. 2012a, 2012b). They confirmed that the AGN energetic contribution to the total power increases with infrared luminosity from $10^{11} L_{\odot} \leq L_{\text{IR}} \leq 10^{12} L_{\odot}$.

Infrared 2.5–5 μm spectroscopy is another powerful tool to study optically elusive buried AGNs in U/LIRGs. One advantage of this band is that dust extinction is much lower than in the optical band (Nishiyama et al. 2009) and is similar to that in the 5–13 μm band (Lutz et al. 1996). Another great advantage is that SB and AGN activity can be distinguished based on the spectral features. First, strong polycyclic aromatic hydrocarbon (PAH) emission, a pure star formation tracer, is located at 3.3 μm in SB galaxies, while pure AGNs exhibit PAH-feature free spectra due to the effects of (1) the X-ray emission destroying the PAHs and (2) the strong continuum emission originating from AGN hot-dust diminishing this feature (Moorwood 1986; Imanishi & Dudley 2000). SB galaxies generally show large 3.3 μm PAH equivalent widths of $\text{EW}_{3.3\text{PAH}} \sim 100$ nm, which never go below 40 nm. Thus, objects with $\text{EW}_{3.3\text{PAH}} \leq 40$ nm may be classified as galaxies that harbor buried AGNs. In SB/AGN composite galaxies, strong PAH emission can be observed because the AGN cannot destroy the PAH molecules located in the outer ($r > 10$ pc) region from the central engine due to shielding by dust and gas. However, strong AGN continuum makes $\text{EW}_{3.3\text{PAH}}$ smaller, well below 40 nm. Using this method, many authors reported the strong sign of buried AGNs in ULIRGs (Imanishi et al. 2006; Sani et al. 2008; Risaliti et al. 2010) and LIRGs (Imanishi et al. 2008, 2010). Another key feature in the 2.5–5 μm band is the continuum slope Γ ($F_{\nu} \propto \lambda^{\Gamma}$). SB galaxies have blue continuum slopes ($\Gamma \sim 0$) in this band owing to the contribution of the stellar photospheric continuum. Conversely, galaxies with AGNs have hot-dust emission heated by AGNs, which produces a red continuum ($\Gamma \geq 1$). This method was first reported by Risaliti et al. (2006) and successfully applied to ULIRGs (Sani et al. 2008; Risaliti et al. 2010) and LIRGs (Imanishi et al. 2008, 2010). Imanishi et al. (2010) combined the two methods ($\text{EW}_{3.3\text{PAH}} \leq 40$ nm and/or $\Gamma > 1$) to find buried AGNs from a sample of U/LIRGs showing no AGN signatures in the optical spectra. They found that the fraction of buried AGNs increases with infrared luminosity in the range of $10^{11} L_{\odot} \leq L_{\text{IR}} \leq 10^{13} L_{\odot}$.

In this paper, we expand the studies of U/LIRGs by Imanishi et al. (2010) into a lower infrared luminosity range, by including normal infrared galaxies (IRGs) with $10^{10} L_{\odot} \leq L_{\text{IR}} < 10^{11} L_{\odot}$, where comprehensive studies are still missing owing to the limited sample. This is because L/IRGs have spatially more extended infrared emission (> 1 kpc, corresponding to $> \text{several arcseconds}$ at $z \sim 0.05$) compared with ULIRGs (Soifer et al. 2001; Imanishi et al. 2011b), and therefore slit spectroscopy with ground-based telescopes could miss their extended emission. Slitless spectroscopy of the Infrared Camera (IRC; Onaka et al. 2007) on board *AKARI* (Murakami et al. 2007) with a $1' \times 1'$ aperture opened a new window to probe such extended emission of L/IRGs. Throughout this paper, we adopt $H_0 = 75 \text{ km s}^{-1} \text{ Mpc}^{-1}$, $\Omega_M = 0.3$, and $\Omega_{\Lambda} = 0.7$ for consistency with the previous publications (Imanishi et al. 2008, 2010).

2. TARGETS

Our motivation is to search for buried AGNs from optically non-Seyfert infrared galaxies and investigate their properties over a wider range of infrared luminosity than in previous studies. An ideal sample can be selected from unbiased catalogs of infrared galaxies with various infrared luminosities at redshifts of $z < 0.45$, where 3.3 μm PAH is detectable in the *AKARI*/IRC 2.5–5.0 μm spectra. To this end, we first gather U/LIRGs with high far-infrared fluxes from *IRAS* catalogs. Our ULIRGs are mainly selected from the bright ULIRG catalog by Klaas et al. (2001), consisting of 41 sources, out of which 25 are optically non-Seyfert galaxies. These ULIRGs have *IRAS* 60 μm fluxes ≥ 3 Jy and far-infrared (40–120 μm) luminosities $L_{40-120 \mu\text{m}} > 10^{12} L_{\odot}$.⁶ In addition to these sources, we also gather 54 fainter, local ($z < 0.45$), optically non-Seyfert ULIRGs from the literature to increase the sample size. The LIRGs are mainly taken from the LIRG catalog of Carico et al. (1988), which is based on the *IRAS* Bright Galaxy catalog. The catalog consists of 61 sources with the criteria of *IRAS* 60 μm fluxes ≥ 5.4 Jy and far-infrared (40–400 μm) luminosities $L_{40-120 \mu\text{m}} > 10^{11} L_{\odot}$. We select 41 optically non-Seyfert galaxies out of this sample. To further increase the number of L/IRG targets, we also utilize the catalog by Spinoglio et al. (2002). They compiled 76 *ISO*-detected sources in the *IRAS* 12 μm galaxy catalog, which gathered all galaxies at Galactic latitudes of $|b| > 25^\circ$ down to the *IRAS* 12 μm flux limit of ≥ 0.22 Jy (Rush et al. 1993). Since AGN tori have peak emission at the MIR band, the 12 μm galaxy catalog could tend to include more AGNs than in far-infrared-selected samples. Indeed, a majority of the members of the Spinoglio et al. (2002) catalog (64 out of 76 sources) are optically Seyfert galaxies. Therefore, we gather the 12 optically non-Seyfert SB galaxies from it. In summary, we select a sufficiently large number of non-Seyfert infrared galaxies (132 sources) as our “parent” sample to be followed up with *AKARI*. The redshifts of all the sources in the above catalogs are distributed within $z < 0.45$.

3. OBSERVATIONS AND DATA REDUCTION

Observation was conducted with the IRC infrared spectrograph (Onaka et al. 2007) on board *AKARI* (Murakami et al. 2007). The spectra in the 2.5–5 μm band were taken with the NG grism mode. This mode achieves an effective spectral resolution of $R \sim 120$ at 3.6 μm , which is sufficient for detecting and tracing the profile of 3.3 μm PAH emission. The IRC has a $1 \times 1 \text{ arcmin}^2$ window with a pixel scale of $1.46 \times 1.46 \text{ arcsec}^2$. All the data were taken as a part of the *AKARI* mission program called “AGNUL” (PI: T. Nakagawa). The observation settings were the same as those described in Chapter 3 of Imanishi et al. (2010). One to seven pointings were assigned for each source according to the brightness. The total on-source exposure time was $\sim \text{six minutes}$ per each pointing. We used IRCZ4 (phase 3; post liquid-He mission) observing mode, where one pointing is composed of eight or nine independent frames (Onaka et al. 2007). This mode successfully removes cosmic-ray contaminations even for sources observed by a single pointing. For sources observed with multiple pointings, we combined all the data to achieve the best signal-to-noise ratio (S/N) after excluding the data sets with particularly bad quality. We often had to discard

⁶ This luminosity is based on the paper of Klaas et al. (2001), where $H_0 = 50 \text{ km s}^{-1} \text{ Mpc}^{-1}$. Therefore, in our study with $H_0 = 75 \text{ km s}^{-1} \text{ Mpc}^{-1}$, some galaxies reach $L_{\text{IR}} = 10^{11.5} L_{\odot}$.

data observed in later epochs of *AKARI*'s phase 3 operation as a result of the increasing background signal.

Spectral analysis was conducted in a standard manner by using the IDL data reduction package for *AKARI* IRC spectra.⁷ The dark subtraction, linearity correction, and flat-field correction were performed using this IDL package. Some infrared galaxies with low luminosities ($L_{\text{IR}} < 10^{12} L_{\odot}$) have spatially extended emission. Hence, we varied the aperture size for spectral extraction according to the actual signal profile of each source. The background was estimated from both sides of the spectral dispersion direction of the target and was subtracted from the source. The IDL package for *AKARI* also performed wavelength and absolute flux calibration. The accuracy of the wavelength calibration is ~ 1 pixel ($\sim 0.01 \mu\text{m}$), and that of the flux calibration is $\sim 10\%$ around the central wavelength of the spectra and up to $\sim 20\%$ at the edges close to $2.5 \mu\text{m}$ and $5.0 \mu\text{m}$.

Out of the 132 sources in our parent sample, we observed 37 objects in total from 2008 June until 2010 February with *AKARI*. After the epoch, *AKARI* fell into the stage where the data highly suffered from the significant background emission. As a result, we could not observe the remaining 95 targets. Also, owing to *AKARI*'s Sun-synchronous polar orbit, higher visibilities were achieved for objects at higher ecliptic latitudes. These observational constraints of *AKARI* make it difficult for us to construct a uniformly flux-limited sample over the entire sky with *AKARI*. However, the observable targets are essentially randomly selected from the parent sample with no selection biases regarding the physical nature of the galaxies. Hence, we regard that our sample has no obvious bias.

Next, we also set the criterion that the averaged S/N for each spectral channel must be higher than five in order to apply our spectral deconvolution analysis. Among the 37 targets observed with *AKARI*, five sources were discarded owing to their low S/N, and the other 10 sources were too faint to be detected. A total of 14 out of 15 nondetected sources are fainter ULIRGs gathered from the literature. These sources have $60 \mu\text{m}$ flux = 1.1 Jy , which is roughly 10 times fainter than that of the detected sources ($f_{60 \mu\text{m}} = 11.8 \text{ Jy}$). Supposing that their infrared spectral energy distribution does not change drastically from that of the detected sources, we can regard that most of the nondetected sources are intrinsically too faint to be observed with *AKARI*/IRC. Figure 1 shows the redshift distribution of the finally selected 22 infrared galaxies.

4. AGN/SB SPECTRAL DECOMPOSITION AND BURIED AGN DIAGNOSTICS

For understanding the properties of buried AGNs in infrared galaxies, it is crucial to analyze the infrared spectra by decomposing SB and AGN components. The $2.5\text{--}5.0 \mu\text{m}$ band covered by *AKARI* IRC has unique advantages for detecting AGN signatures. As introduced in Section 1, one promising method for finding buried AGNs is the strength (equivalent width) of the $3.3 \mu\text{m}$ PAH emission as proposed by Imanishi & Dudley (2000). Pure SB galaxies show generally strong $3.3 \mu\text{m}$ PAH emission with $\text{EW}_{3.3\text{PAH}} \sim 100 \text{ nm}$ because plenty of SB-produced UV photons excite PAH molecules (Mouri et al. 1990). By contrast, if an AGN resides in the galaxy, the PAH feature becomes weaker, $\text{EW}_{3.3\text{PAH}} < 40 \text{ nm}$ (Imanishi & Dudley 2000). Imanishi et al. (2008, 2010) also used the red continuum slope ($\Gamma > 1$ for

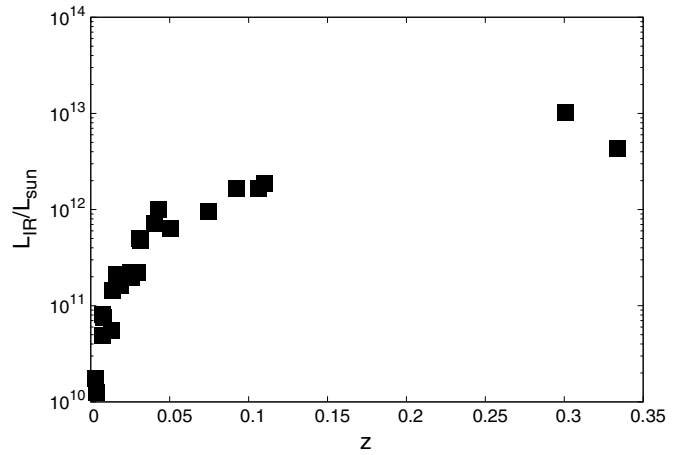


Figure 1. Redshift vs. infrared luminosity plot for the 22 infrared galaxies in our sample.

$F_{\nu} \propto \lambda^{\Gamma}$) for finding buried AGNs. In this paper, we develop the previous works not only to find buried AGNs but also to quantitatively estimate their energy contribution by performing detailed spectral fitting with a continuum model consisting of a stellar component and dust components from AGNs and/or SBs. Emission- and absorption-line features are also included in the model.

4.1. AGN-Heated Dust Component

The AGN emission in the near- to mid-infrared originates from the radiation reprocessed by hot dust in the torus. Recent studies of dusty torus models reproduce the observed nuclear mid-infrared emission well by assuming that the torus media have a clumpy structure (e.g., Nenkova et al. 2008a, 2008b; Ramos Almeida et al. 2009, 2011; Alonso-Herrero et al. 2011). However, some authors mentioned that there are difficulties in fitting their near-infrared spectral energy distribution (SED; Stalevski et al. 2012; Lira et al. 2013; Videla et al. 2013). This is due to the complicated degeneracies, including the possible existence of an extra hot-dust ($\sim 1500 \text{ K}$) component originating from the vicinity of the AGN (Kishimoto et al. 2011), and/or contamination from the host galaxies, and/or the extinction of the torus emission by interstellar matter in the host galaxies. In this work, we take the simplest approach to approximate the torus dust emission by a single blackbody component, considering our limited wavelength range. Presumably, the dusty torus has a continuous dust temperature distribution and produces emission peaked around $\sim 10 \mu\text{m}$. Hence, our single blackbody fit should trace its peak temperature at $\sim 300 \text{ K}$. Accordingly, we set a conservative upper limit on its temperature as $T_{\text{dust}} < 800 \text{ K}$ (Oyabu et al. 2011).

4.2. Stellar and Starburst Component

The stellar photospheric emission in the host galaxy contributes to the total radiation in the $2.5\text{--}5.0 \mu\text{m}$ spectral range. This component produces a decreasing continuum flux at $\geq 1.8 \mu\text{m}$ (Sawicki 2002). We first determine the temperature $T^{(\text{stellar})}$ by fitting the Two Micron All Sky Survey (2MASS) J , H , and K_s photometric data with a blackbody model, and we fix the temperature at its best-fit value when analyzing the *AKARI* $2.5\text{--}5.0 \mu\text{m}$ spectra. For Mrk 551 and Mrk 848, we cannot find any 2MASS fluxes. Therefore, we use the J , H , and K photometric data from the literature (Spinoglio et al. 1995)

⁷ The software package is available through the *AKARI* data reduction webpage <http://www.ir.isas.jaxa.jp/AKARI/Observation/>. For the details of the data analysis, see Ohya et al. (2007).

instead of the 2MASS data. SBs produce a large amount of dust, which generally has lower temperatures than those of the AGN-heated dust, typically $T^{(\text{dust})} < 100$ K (Sanders & Mirabel 1996). As already suggested by Sawicki (2002) and many other studies, such cold dust with $T^{(\text{dust})} < 100$ K does not significantly contribute to the $2.5\text{--}5.0\ \mu\text{m}$ spectra, and therefore we ignore the contribution from the SB dust emission. However, some SB galaxies show excess emission from very hot dust with a temperature of $\sim 10^3$ K, requiring at least two blackbody components. This very hot dust component of $\sim 10^3$ K would not originate from the dusty torus, from which blackbody radiation of ~ 300 K is generally expected (see Section 4.1). One possible origin is the emission mainly heated by massive stars in H II regions (Hunt et al. 2002; Lu et al. 2003; Siebenmorgen 1993). If such emission is required from the data, we model it with a single blackbody with a temperature of $T_{\text{H II}} \sim 1000$ K in a range of $800\text{ K} < T_{\text{H II}} < 1200$ K, as suggested by Hunt et al. (2002).

4.3. Emission and Absorption Lines

The $2.5\text{--}5.0\ \mu\text{m}$ spectra of infrared galaxies contain various emission/absorption-line features. The previous studies of the AKARI “AGNUL” program (Imanishi et al. 2008, 2010) reported three PAH lines at 3.3 , 3.4 , and $3.5\ \mu\text{m}$, hydrogen Brakett series at $4.05\ \mu\text{m}$ Br α and $2.63\ \mu\text{m}$ Br β , and Pfund series at $4.65\ \mu\text{m}$ Pf β and $3.74\ \mu\text{m}$ Pf γ as emission lines. They also reported absorption features at $3.1\ \mu\text{m}$ by H_2O ice, at $4.29\ \mu\text{m}$ by CO_2 , and at $4.67\ \mu\text{m}$ by CO. Because PAH emission is believed to originate from solid-state molecules, the line profile becomes Lorentzian (Yamada et al. 2013). For simplicity, however, we model all the lines, including those of PAH by Gaussian profiles, following Imanishi et al. (2010). The central wavelength and line width are fixed within a spectral resolution at appropriate values reported in the literature.

4.4. Total Model Spectra

We thus construct a spectral model consisting of the multiple continuum components over which the emission/absorption lines are superposed. For the continuum we consider three blackbody components, (1) a direct stellar component $f_{\text{BB}}^{(\text{stellar})}$, (2) a dust component from AGNs with a temperature below 800 K $f_{\text{BB}}^{(\text{dust})}$, and (3) a very hot ($800\text{--}1200$ K) dust component from H II regions $f_{\text{BB}}^{(\text{H II})}$. Each blackbody component has two parameters, normalization ($C^{(\text{stellar})}$, $C^{(\text{dust})}$, $C^{(\text{H II})}$) and temperature ($T^{(\text{stellar})}$, $T^{(\text{dust})}$, $T^{(\text{H II})}$), which, except for $T^{(\text{stellar})}$, are left as free parameters in the spectral fit.

Previous studies suggest that emission from warm dust may be partly absorbed by outer cold dust (e.g., Risaliti et al. 2010; Imanishi et al. 2010). To take this into account, we apply an extinction correction by incorporating $\tau(\lambda)$ into the blackbody components. We adopt the dust extinction index of $\beta = 1.75$ (Draine 1989; Hunt et al. 2002) as

$$\tau(\lambda) = \tau_0 \left(\frac{\lambda}{\mu\text{m}} \right)^{-1.75}. \quad (1)$$

The normalization value τ_0 can be estimated from the optical thickness of $3.1\ \mu\text{m}$ ice (τ_{ice}), which is calculated by using the deconvolved continuum from the dust ($f_{\text{BB}}^{(\text{dust})}$). Imanishi & Maloney (2003) estimated the relationship between the dust extinction A_V and τ_{ice} with

$$\tau_{\text{ice}} = 0.06 A_V (1 + f), \quad (2)$$

where f is the fraction of dust that is covered with an ice mantle. The maximum value of f is derived to be 0.3 in the core of U/LIRGs in Imanishi & Maloney (2003). From the relation between the optical thickness and extinction with $\tau_V = A_V/1.08$ and Equation (2) with $f = 0.3$,

$$\tau_V = \frac{\tau_{\text{ice}}}{0.06 \times 1.3 \times 1.08} = 11.87 \tau_{\text{ice}} \quad (3)$$

is derived. By combining Equations (1) and (3), at the V band ($0.55\ \mu\text{m}$),

$$\tau(\lambda = 0.55\ \mu\text{m}) = \tau_0 \times 0.55^{-1.75} = 11.87 \tau_{\text{ice}} \quad (4)$$

$$\Longleftrightarrow \tau_0 = 4.3 \tau_{\text{ice}}. \quad (5)$$

Accordingly, we model the observed component as $f_{\text{BBobs}}^{(\text{dust})} = f_{\text{BB}}^{(\text{dust})}(\lambda) \times e^{-\tau(\lambda)}$, where $\tau(\lambda) = 4.3 \times \tau_{\text{ice}} \times (\lambda/\mu\text{m})^{-1.75}$.

First, we adopt only two continuum components of direct stellar emission and AGN/SB dust emission to fit the observed spectra, because the contribution of dust emission from H II regions is not always required from the data. This model (two-component model) is written as

$$f_{\text{model}}(\lambda) = f_{\text{BB}}^{(\text{stellar})}(\lambda) + f_{\text{BBobs}}^{(\text{dust})}(\lambda) + \sum_i f_i^{(\text{line})}(\lambda), \quad (6)$$

where $f_i^{(\text{line})}(\lambda)$ represents each line’s profile as described in Section 4.3. In some cases, mainly for sources showing little contribution from $f_{\text{BB}}^{(\text{dust})}$, the two-component model given by Equation (6) does not fit the data well. Then, we add the $f_{\text{BB}}^{(\text{H II})}$ component to the above model:

$$f_{\text{model}}(\lambda) = f_{\text{BB}}^{(\text{stellar})}(\lambda) + f_{\text{BB}}^{(\text{H II})}(\lambda) + f_{\text{BBobs}}^{(\text{dust})}(\lambda) + \sum_i f_i^{(\text{line})}(\lambda). \quad (7)$$

We adopt this model (three-component model) only when the fitting result is significantly improved from the two-component model with a $> 95\%$ confidence level on the basis of an F -test. The fitting model we adopt for each source is summarized in Table 1. As shown in Figure 2, all sources that require the three components are galaxies showing blue continua in their spectra (e.g., NGC 4818). As many authors (e.g., Risaliti et al. 2010; Imanishi et al. 2010) suggested, these galaxies do not show buried AGN signs but are more likely normal SB galaxies. This is consistent with our assumption that the extra hot ($T \sim 10^3$ K) component should originate from H II regions, not from the AGN torus.

5. RESULTS AND DISCUSSIONS

5.1. AKARI Spectra and AGN Diagnostics

Figure 2 displays the observed AKARI spectra of all 22 sources (red dots with flux error bars) overplotted with their best-fit models (blue line). Each line/continuum component is also plotted in the figure. As noticed, a majority of sources show $3.3\ \mu\text{m}$ PAH emission features. Tables 2 and 3 summarize the fitting results.

For finding buried AGNs, we apply two AGN diagnostics: (1) PAH emission line and (2) torus-dust continuum. The PAH

Table 1
Basic Information of Our Sample

Name (1)	ObsID (2)	z (3)	f_{12} (4)	f_{25} (5)	f_{60} (6)	f_{100} (7)	$\log L_{\text{IR}}$ (8)	Components (9)
ESO 286-IG19	1122176-001	0.043	0.28	1.90	12.71	10.58	12.00	2comp
IC 5135	1120236-001	0.016	0.63	2.14	16.67	26.27	11.33	2comp
IRAS 03068-5346	1122105-001	0.074	0.25	0.20	3.43	3.92	11.98	2comp
IRAS 03538-6432	1122106-001	0.30	0.25	0.25	0.96	1.54	13.01	2comp
IRAS 10494+4424	1122096-001	0.092	0.25	0.25	3.36	5.60	12.22	2comp
IRAS 17028+5817	1122101-001	0.11	0.25	0.08	2.49	4.05	12.22	2comp
IRASF 07353+2903	1120200-001	0.33	0.08	0.10	0.22	0.64	12.63	2comp
MCG +02-04-025	1122123-001	0.031	0.37	1.46	11.13	10.29	11.67	2comp
MCG +08-23-097	1122130-001	0.029	0.25	0.53	5.08	8.10	11.34	2comp
MCG +10-19-057	1122132-001	0.031	0.40	1.92	11.35	10.81	11.70	2comp
Mrk 1490	1122134-001	0.026	0.25	0.86	6.21	8.38	11.30	3comp
Mrk 551	1122171-001	0.050	0.26	0.80	4.63	6.13	11.80	2comp
Mrk 848	1122136-001	0.040	0.32	1.52	9.38	10.26	11.86	2comp
NGC 2339	1120230-001	0.0074	0.53	2.11	18.96	32.24	10.69	3comp
NGC 2388	1120231-001	0.014	0.49	1.99	16.21	23.09	11.15	3comp
NGC 4102	1120232-001	0.0028	1.45	6.83	47.37	68.50	10.25	2comp
NGC 4194	1122091-001	0.0083	0.86	4.36	22.79	25.94	10.88	3comp
NGC 4818	1120234-001	0.0036	0.85	3.88	20.26	26.55	10.10	3comp
NGC 520	1120229-001	0.0076	0.78	2.83	31.52	48.40	10.91	3comp
NGC 6285	1122138-001	0.019	0.30	0.44	7.43	23.58	11.21	3comp
NGC 838	1122173-001	0.013	0.59	1.83	0.40	17.94	10.74	3comp
ZW 453.062	1122140-001	0.025	0.29	0.57	7.59	11.04	11.34	2comp

Notes. Columns 1: object name; 2: observation ID of *AKARI*; 3: redshift; 4–7: 12, 25, 60, and 100 μm *IRAS* flux density in units of Jansky (Jy); 8: total infrared (8–1000 μm) luminosity in units of solar luminosity (L_{\odot}), calculated from $L_{\text{IR}} = 2.1 \times 10^{39} \times D(\text{Mpc})^2 \times (13.48 f_{12} + 5.16 f_{25} + 2.58 f_{60} + f_{100})$ (Sanders & Mirabel 1996); 9: number of continuum components adopted to fit each spectrum; “2comp” and “3comp” correspond to the model spectra given by Equations (6) and (7) in Section 4.4, respectively. In the case of “3comp,” the main flux contribution originates from stellar and H II components with little contribution from the dust component. This is why for “3comp” sources the dust component (dot-dashed line) is hardly seen in Figure 2.

Table 2
Fitting Properties and AGN Signs Obtained from the *AKARI* 2.5–5.0 μm Spectroscopy

Name (1)	$\text{EW}_{3.3\text{PAH}}$ (2)	$T^{(\text{stellar})}$ (3)	$T^{(\text{H II})}$ (4)	$T^{(\text{dust})}$ (5)	AGN sign (EW) (6)	AGN sign (red) (7)
ESO 286-IG19	68.9 ± 5.2	2786 ± 94	...	358 ± 4	N	Y
IC 5135	47.3 ± 1.2	2929 ± 37	...	749 ± 20	N	Y
IRAS 03068-5346	90.4 ± 5.7	3148 ± 411	...	700 ± 82	N	Y
IRAS 03538-6432	31.9 ± 4.9	1475 ± 80	...	304 ± 15	Y	Y
IRAS 10494+4424	81.2 ± 4.8	2083 ± 144	...	415 ± 22	N	Y
IRAS 17028+5817	54.2 ± 4.5	2206 ± 199	...	366 ± 17	N	Y
IRASF 07353+2903	5.2 ± 3.9	1544 ± 154	...	249 ± 56	Y	Y
MCG +02-04-025	121.3 ± 5.0	2545 ± 86	...	349 ± 11	N	Y
MCG +08-23-097	41.4 ± 1.6	2612 ± 74	...	649 ± 64	N	Y
MCG +10-19-057	76.1 ± 3.0	2455 ± 68	...	708 ± 71	N	Y
Mrk 1490	59.7 ± 1.6	2568 ± 70	1128 ± 94	<100	N	N
Mrk 551	41.5 ± 2.8	2545 ± 141	...	499 ± 13	N	Y
Mrk 848	93.9 ± 4.2	3142 ± 227	...	715 ± 43	N	Y
NGC 2339	42.3 ± 1.4	2968 ± 41	1199 ± 275	<100	N	N
NGC 2388	55.3 ± 1.1	2715 ± 37	1177 ± 95	<100	N	N
NGC 4102	38.7 ± 1.7	2971 ± 44	...	739 ± 27	Y	Y
NGC 4194	78.2 ± 1.8	2986 ± 46	1192 ± 68	<100	N	N
NGC 4818	42.0 ± 1.3	3240 ± 61	1200 ± 217	<100	N	N
NGC 520	54.2 ± 1.1	2897 ± 55	1149 ± 75	<100	N	N
NGC 6285	59.9 ± 2.1	2940 ± 83	1173 ± 194	<100	N	N
NGC 838	110.9 ± 1.2	2863 ± 41	1200 ± 185	<100	N	N
ZW 453.062	50.9 ± 3.2	2725 ± 55	...	649 ± 71	N	Y

Notes. Table 2 summarizes the observed properties of the 22 sources obtained from the *AKARI* spectroscopy. Columns 1: object name; 2: equivalent width of 3.3 μm PAH emission; 3–5: temperature of blackbody originated from stellar emission, H II emission, and dust emission, respectively (see Section 4 for details); 6: AGN sign based on the PAH diagnostic: “Y” signifies that the source has buried-AGN sign ($\text{EW}_{3.3\text{PAH}} < 40 \text{ nm}$), while “N” represents no AGN sign ($\text{EW}_{3.3\text{PAH}} > 40 \text{ nm}$); 7: AGN sign based on the hot-dust diagnostic: “Y” represents the source with $T^{(\text{dust})} > 200 \text{ K}$, while “N” represents the source with $T^{(\text{dust})} < 200 \text{ K}$.

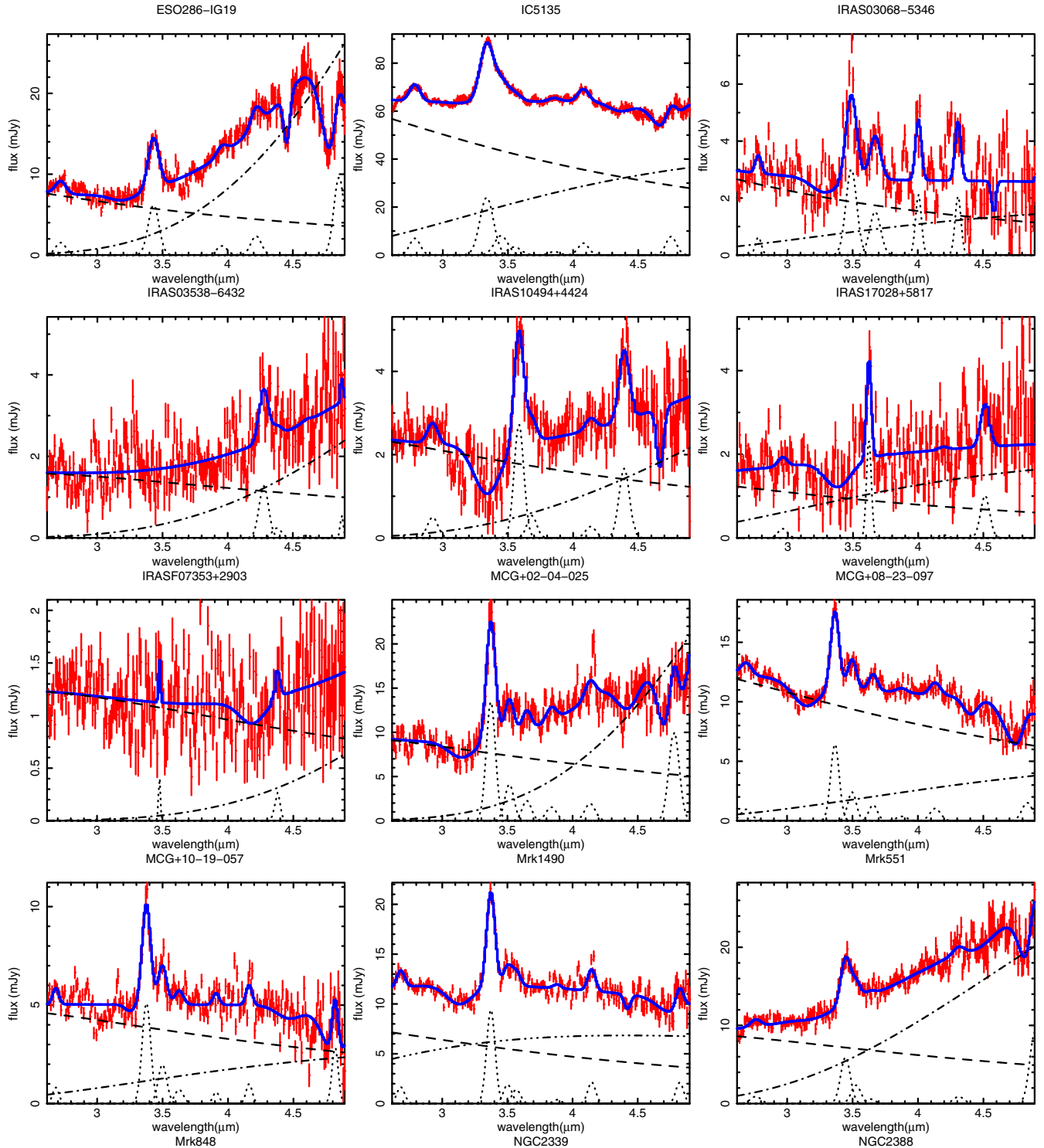


Figure 2. *AKARI* 2.5–5.0 μm spectra (red dots with error bars) of the 22 infrared galaxies overplotted with the best-fit models (blue solid curve). The black dashed, triple-dot-dashed, and dot-dashed curves represent the stellar, H II, and AGN/SB dust components, respectively. Black dotted curves represent emission lines.

(A color version of this figure is available in the online journal.)

diagnostic is based on $\text{EW}_{3.3\text{PAH}}$, as discussed in Section 4; we identify a buried AGN if it shows a small 3.3 μm PAH equivalent width with $\text{EW}_{3.3\text{PAH}} < 40$ nm. The torus-dust diagnostic is based on whether or not there is a contribution from a hot dust component from the torus; we set the criterion of identifying buried AGNs as $T^{(\text{dust})} > 200$ K.

In the left panel of Figure 3, we present the two AGN diagnostic diagrams applied for our sample, where ULIRGs,

LIRGs, and IRGs are plotted as pink circles, red triangles, and brown squares, respectively. There is a clear boundary of distribution of the dust temperature around $T^{(\text{dust})} \sim 200$ K. This supports our criterion that AGNs should have high dust temperatures ($T^{(\text{dust})} > 200$ K) and are well distinguishable from SBs. Interestingly, many infrared galaxies with large PAH equivalent widths ($\text{EW}_{3.3\text{PAH}} > 40$ nm) show high dust temperatures ($T^{(\text{dust})} > 200$ K). One reason could be that because

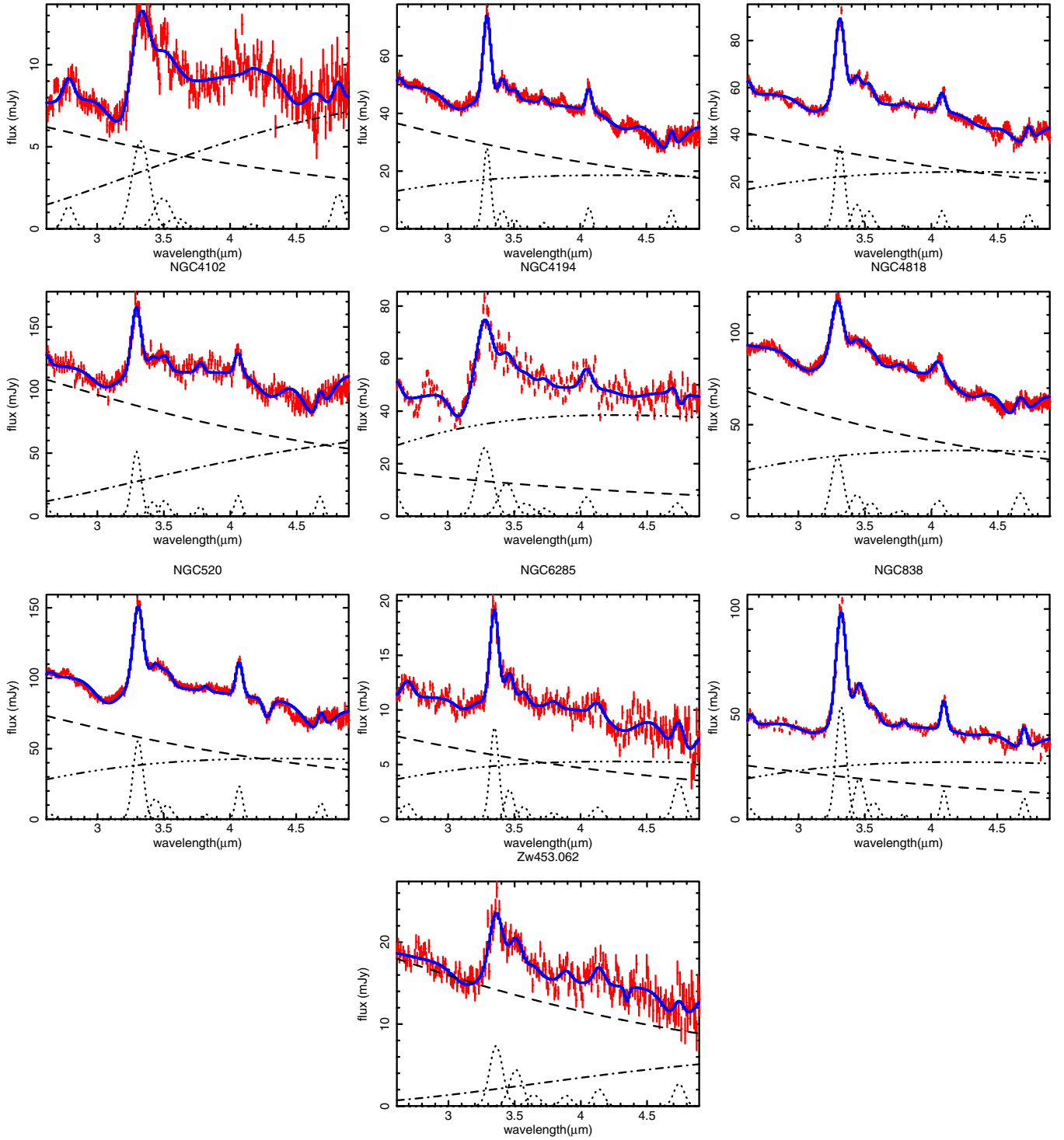


Figure 2. (Continued)

of the large aperture of *AKARI*/IRC and less luminous nucleus emission in these galaxies, the spectra contain a relatively large contribution of $3.3\ \mu\text{m}$ PAH emission in the host galaxies where PAH molecules are not destroyed by AGN X-ray photons. This effect works to increase the PAH equivalent width, and hence the PAH diagnostic could miss buried AGNs. By contrast, the hot-dust diagnostic is not subject to the aperture effect because the continuum emission can be properly decomposed by the spectral fit. In fact, the torus-dust AGN diagnostic can recover all the buried AGNs identified by the

PAH diagnostic; in other words, there is no source with a low dust temperature ($T_{\text{dust}}^{(\text{dust})} < 200\ \text{K}$) and a small PAH equivalent width ($\text{EW}_{3.3\text{PAH}} < 40\ \text{nm}$) in our sample. This supports the superiority of using the hot-dust diagnostic for finding AGNs completely.

The right panel of Figure 3 shows the plot of $\text{EW}_{3.3\text{PAH}}$ versus dust luminosity ($L_{\text{BB}}^{(\text{dust})}$) tabulated in Tables 2 and 3. In the figure, we plot only the sources with $T > 200\ \text{K}$. This is because the $2.5\text{--}5.0\ \mu\text{m}$ spectral range is not sensitive to the dust emission with low temperature $T < 100\ \text{K}$. In this case,

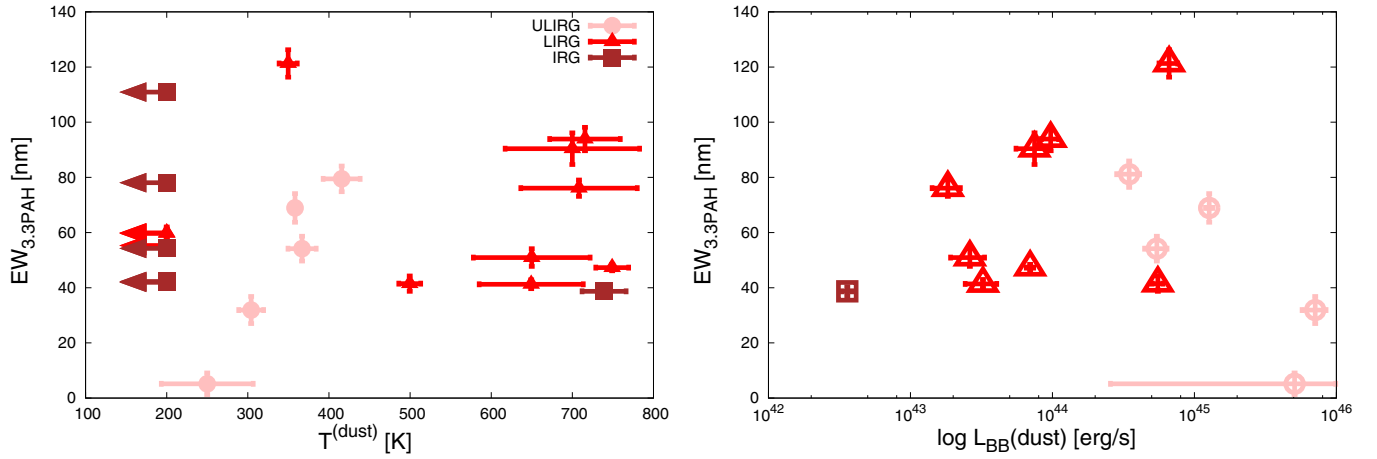


Figure 3. Plot of equivalent width of $3.3\ \mu\text{m}$ PAH emission ($\text{EW}_{3.3\text{PAH}}$) vs. dust temperature $T^{(\text{dust})}$ (left panel) and infrared AGN luminosity (right panel). Pink circles, red triangles, and brown squares represent ULIRGs, LIRGs, and IRGs, respectively. In the right panel, we plot only the sources with $T^{(\text{dust})} > 200\ \text{K}$ because those with $T^{(\text{dust})} < 200\ \text{K}$ have a great temperature uncertainty, and therefore the luminosity is given only the small upper limit with $10^{40}\ \text{erg s}^{-1}$ (see the discussion in Section 5.1).

(A color version of this figure is available in the online journal.)

Table 3
Observed Properties Obtained from the *AKARI* 2.5–5.0 μm Spectroscopy

Name (1)	$f_{\text{BB}}^{(\text{stellar})}$ (2)	$f_{\text{BB}}^{(\text{H II})}$ (3)	$f_{\text{BB}}^{(\text{dust})}$ (4)	$f_{3.3\text{PAH}}$ (5)	τ_{ice} (6)	$\log L_{\text{BB}}^{(\text{stellar})}$ (7)	$\log L_{\text{BB}}^{(\text{H II})}$ (8)	$\log L_{\text{BB}}^{(\text{dust})}$ (9)	$\log L_{3.3\text{PAH}}$ (10)	$L_{\text{BB}}^{(\text{dust})}/L_{\text{IR}}$ (11)
ESO 286-IG19	112 ± 4	...	338 ± 21	1.58 ± 0.12	0.13 ± 0.05	44.62 ± 0.01	...	45.10 ± 0.03	41.77 ± 0.03	0.329 ± 0.020
IC 5135	856 ± 12	...	137 ± 9	8.66 ± 0.21	<0.02	44.64 ± 0.01	...	43.84 ± 0.03	41.65 ± 0.01	0.085 ± 0.005
IRAS 03068-5346	54 ± 7	...	7 ± 2	0.75 ± 0.05	0.20 ± 0.07	44.80 ± 0.06	...	43.87 ± 0.13	41.95 ± 0.03	0.020 ± 0.005
IRAS 03538-6432	16 ± 1	...	29 ± 6	0.15 ± 0.02	<0.09	45.60 ± 0.02	...	45.85 ± 0.09	42.58 ± 0.07	0.180 ± 0.034
IRAS 10494+4424	25 ± 2	...	19 ± 4	0.56 ± 0.03	1.02 ± 0.08	44.66 ± 0.03	...	44.54 ± 0.09	42.02 ± 0.03	0.055 ± 0.010
IRAS 17028+5817	21 ± 2	...	22 ± 4	0.26 ± 0.02	0.30 ± 0.12	44.70 ± 0.04	...	44.74 ± 0.09	41.82 ± 0.04	0.085 ± 0.015
IRAS F07353+2903	15 ± 2	...	16 ± 15	0.02 ± 0.01	0.38 ± 0.21	45.66 ± 0.07	...	45.71 ± 1.30	41.74 ± 0.62	0.308 ± 0.292
MCG +02-04-025	114 ± 4	...	340 ± 52	3.20 ± 0.13	0.27 ± 0.06	44.35 ± 0.01	...	44.82 ± 0.07	41.80 ± 0.02	0.366 ± 0.055
MCG +08-23-097	153 ± 5	...	19 ± 5	1.41 ± 0.06	0.39 ± 0.04	44.42 ± 0.01	...	43.51 ± 0.13	41.39 ± 0.02	0.038 ± 0.010
MCG +10-19-057	54 ± 2	...	10 ± 3	1.11 ± 0.04	0.08 ± 0.06	44.02 ± 0.01	...	43.26 ± 0.11	41.33 ± 0.02	0.010 ± 0.002
Mrk 1490	89 ± 7	33 ± 4	...	2.04 ± 0.06	...	44.07 ± 0.04	43.64 ± 0.05	...	41.43 ± 0.01	...
Mrk 551	113 ± 6	...	106 ± 10	1.39 ± 0.09	<0.03	44.77 ± 0.02	...	44.74 ± 0.04	41.86 ± 0.03	0.228 ± 0.020
Mrk 848	117 ± 9	...	30 ± 5	2.43 ± 0.11	0.18 ± 0.03	44.58 ± 0.03	...	43.99 ± 0.06	41.90 ± 0.02	0.035 ± 0.005
NGC 2339	526 ± 33	101 ± 25	...	5.68 ± 0.19	...	43.74 ± 0.03	43.02 ± 0.12	...	40.77 ± 0.01	...
NGC 2388	534 ± 26	120 ± 13	...	8.88 ± 0.17	...	44.30 ± 0.02	43.65 ± 0.05	...	41.52 ± 0.01	...
NGC 4102	1629 ± 26	...	235 ± 20	13.10 ± 0.56	0.20 ± 0.03	43.40 ± 0.01	...	42.56 ± 0.04	40.30 ± 0.02	0.053 ± 0.004
NGC 4194	257 ± 26	193 ± 13	...	11.11 ± 0.26	...	43.54 ± 0.05	43.41 ± 0.03	...	41.18 ± 0.01	...
NGC 4818	1191 ± 54	181 ± 35	...	10.43 ± 0.33	...	43.46 ± 0.02	42.64 ± 0.09	...	40.40 ± 0.01	...
NGC 520	1052 ± 42	206 ± 19	...	15.10 ± 0.31	...	44.07 ± 0.02	43.36 ± 0.04	...	41.23 ± 0.01	...
NGC 6285	120 ± 13	26 ± 6	...	1.86 ± 0.07	...	43.93 ± 0.05	43.25 ± 0.11	...	41.12 ± 0.02	...
NGC 838	370 ± 28	137 ± 22	...	14.55 ± 0.15	...	44.07 ± 0.03	43.64 ± 0.08	...	41.67 ± 0.01	...
ZW 453.062	245 ± 6	...	21 ± 6	2.47 ± 0.16	0.32 ± 0.07	44.49 ± 0.01	...	43.42 ± 0.14	41.49 ± 0.03	0.031 ± 0.008

Notes. Table 3 summarizes the observed properties including continuum fluxes and luminosities of the 22 sources obtained from the *AKARI* spectroscopy. Columns 1:s object name; 2–4) flux of the stellar, H II, and AGN blackbody component in units of $10^{-12}\ \text{erg cm}^{-2}\ \text{s}^{-1}$, respectively; 5: $3.3\ \mu\text{m}$ PAH flux in units of $10^{-13}\ \text{erg cm}^{-2}\ \text{s}^{-1}$; 6: optical thickness of H_2O ice; 7–9: logarithmic luminosity of the stellar, H II, and dust-torus blackbody component in units of erg s^{-1} , respectively; 10: logarithmic luminosity of the $3.3\ \mu\text{m}$ PAH emission in units of erg s^{-1} ; 11: ratio of the AGN blackbody luminosity to the total infrared luminosity.

only an upper limit of the dust luminosity can be derived. This is the reason why the dust luminosity with $T^{(\text{dust})} < 200\ \text{K}$ is very small, $L_{\text{BB}}^{(\text{dust})} \ll 10^{40}\ \text{erg s}^{-1}$. The figure shows that all the sources with $T^{(\text{dust})} > 200\ \text{K}$ have significant dust emission with $L_{\text{BB}}^{(\text{dust})} > 10^{42}\ \text{erg s}^{-1}$. Thus, the alternative criterion for detecting AGNs can be $L_{\text{BB}}^{(\text{dust})} > 10^{42}\ \text{erg s}^{-1}$ instead of $T^{(\text{dust})} > 200\ \text{K}$. In summary, we conclude that the hot-dust AGN diagnostic is a better method for finding buried AGNs in the *AKARI* IRC band.

5.2. Buried AGN Contribution as a Function of Infrared Luminosity

One motivation of our study is to reveal how frequently buried AGNs exist in infrared galaxies. Figure 4 shows the fraction of buried AGNs as a function of infrared luminosity. The left and right panels show the results based on the PAH AGN diagnostic and on the torus-dust AGN diagnostic, respectively. As discussed above, the latter diagnostic is more complete than the former for finding buried AGNs from

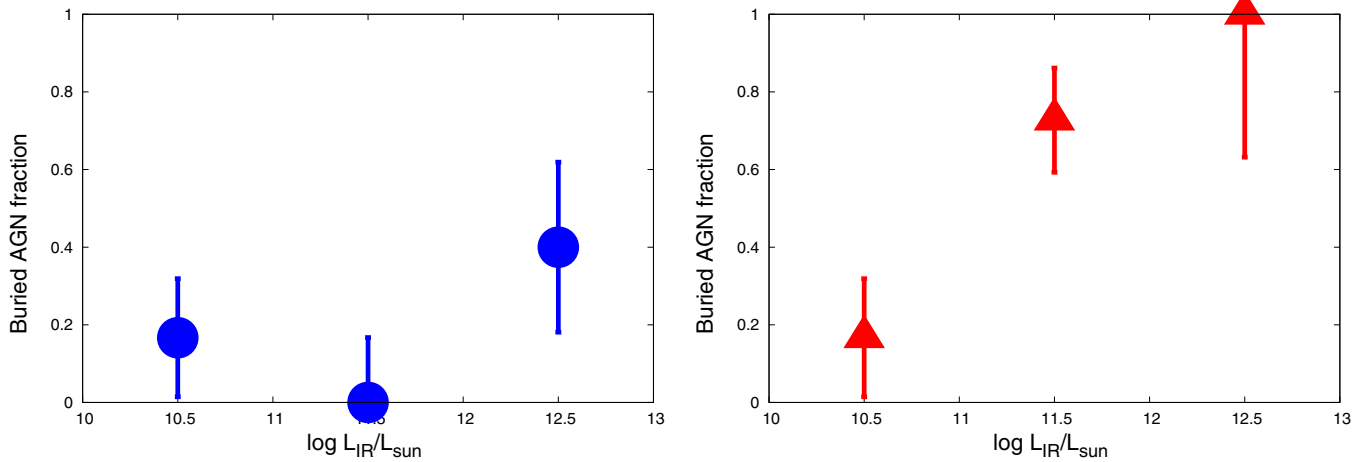


Figure 4. Buried AGN fraction as a function of infrared luminosity. The left panel shows the result based on the $3.3\ \mu\text{m}$ PAH AGN diagnostic, and the right panel shows that based on the torus-dust AGN diagnostic.

(A color version of this figure is available in the online journal.)

infrared galaxies. Therefore, we discuss the result of the right panel hereafter.

In total, we detect 14 buried AGNs out of the 22 infrared galaxies without any AGN signs in the optical band. We also find a clear trend that the fraction of buried AGNs increases with infrared luminosity. While only 17% (one out of six sources) of the IRGs contain buried AGNs, the U/LIRGs contain them almost ubiquitously ($8/11 = 72\%$ for LIRGs and $5/5 = 100\%$ for ULIRGs). Our results for U/LIRGs are consistent with those obtained by Imanishi et al. (2010) within the statistical uncertainties. Although most of the IRGs are selected from the $12\ \mu\text{m}$ galaxy catalog, which is sensitive to torus-dust emission, an AGN is detected only from one source out of the five targets.

The high AGN fraction in U/LIRGs may be related to their high merger rates. There is strong observational evidence that most U/LIRGs have experienced merging or strong galaxy–galaxy interactions (Veilleux et al. 2002). The mergers can induce strong SBs within the galaxies, which also makes galactic gas fall into the galactic center and trigger AGN activity obscured by dust (Sanders et al. 1988; Mihos & Hernquist 1996; Di Matteo et al. 2005; Hopkins et al. 2006). Sanders & Ishida (2004) show that infrared galaxies with signs of recent merger drastically increase at $L_{\text{IR}} \sim 10^{11.2} L_{\odot}$ toward a higher luminosity range. This result is in accordance with our finding that the buried AGN fraction drastically increases from $L_{\text{IR}} \sim 10^{11} L_{\odot}$.

We confirm the dependence of the AGN fraction on luminosity by investigating the ratio between the $3.3\ \mu\text{m}$ PAH luminosity ($L_{3.3\text{PAH}}$) and total infrared luminosity L_{IR} . Pure SB galaxies generally have a constant ratio $L_{3.3\text{PAH}}/L_{\text{IR}} \sim 10^{-3}$. If an AGN exists inside the galaxy, the ratio becomes smaller because X-rays from the AGN destroy PAH molecules and the infrared continuum luminosity is increased by the torus-dust emission. Figure 5 plots $L_{3.3\text{PAH}}/L_{\text{IR}}$ as a function of infrared luminosity for our sample. As noted, it decreases with infrared luminosity, especially at $L_{\text{IR}} > 2 \times 10^{11} L_{\odot}$. We also find that the sources with small $L_{3.3\text{PAH}}/L_{\text{IR}}$ ratios match those with buried AGN signs, supporting the above idea. Note that there is a possibility that this trend may be caused by the destruction of small PAH molecules by major mergers (Yamada et al. 2013) rather than by AGNs. Nevertheless, since all the sources with $L_{3.3\text{PAH}}/L_{\text{IR}} < \sim 10^{-4}$ show buried AGN signs, the conserva-

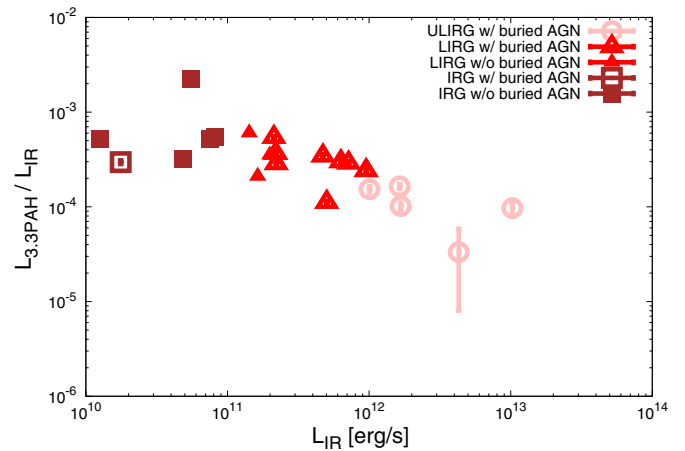


Figure 5. Ratio of $L_{3.3\text{PAH}}/L_{\text{IR}}$ as a function of infrared luminosity. Open circles/triangles/squares represent ULIRGs/LIRGs/IRGs with AGN signs, respectively. Filled triangle/square represents LIRGs/IRGs without AGN signs, respectively. Note that all ULIRGs in our sample are diagnosed to have buried AGNs.

(A color version of this figure is available in the online journal.)

tive criterion $L_{3.3\text{PAH}}/L_{\text{IR}} < 10^{-4}$ could be phenomenologically used as another diagnostic for finding buried AGNs.

5.3. Luminosity Contribution of Buried AGNs to the Total Infrared Luminosity

Our second motivation is to determine the energetic importance of AGNs in these infrared galaxies. As discussed in Section 5.1, the luminosity contribution from dust blackbody component ($L_{\text{BB}}^{(\text{dust})}$) predominantly originates from AGN-heated dust, and the luminosity contribution of SB-heated dust to $L_{\text{BB}}^{(\text{dust})}$ is negligible. Thus, using the best-fit blackbody parameters obtained by the spectral fit, we can estimate the total luminosity from AGN-heated dust and hence its ratio to the total infrared luminosity. Figure 6 shows the averaged fraction of AGN power to the total infrared luminosity for IRGs, LIRGs, and ULIRGs. As noticed, the AGN contribution increases with infrared luminosity, while the values are quite small, $\sim 0.9 \pm 0.8\%$ in IRGs, $\sim 7.4 \pm 3.3\%$ in LIRGs, and $\sim 19.1 \pm 5.0\%$ in ULIRGs.

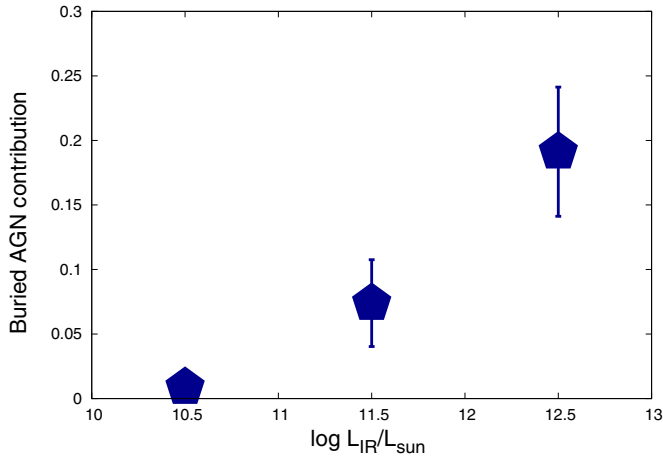


Figure 6. Energy contribution of buried AGNs to the total infrared luminosity as a function of infrared luminosity.

(A color version of this figure is available in the online journal.)

This suggests that the bulk of the infrared emission originates from SBs, not from AGNs in these galaxies. One caveat for this result is that we cannot completely exclude the possibility that the estimated luminosity of $L_{\text{BB}}^{(\text{Hn})}$ might be partially originated from the torus dust if it has an extreme temperature distribution. We thus calculate the averaged $L_{\text{BB}}^{(\text{Hn})}/L_{\text{IR}}$ ratio to check whether it could have a significant contribution. We find $L_{\text{BB}}^{(\text{Hn})}/L_{\text{IR}} \sim 7\%$, suggesting that the main results above would not be affected, even if the observed very hot (>1000 K) dust component were totally due to the AGN emission.

Another caveat for interpreting this result is the selection bias for our sample, which consists of optically non-Seyfert galaxies. Previous studies based on samples including optically Seyfert AGNs found larger average AGN contribution to the total infrared luminosity, 10%–15% in LIRGs (Petric et al. 2011; Alonso-Herrero et al. 2012) and 15%–40% in ULIRGs (Veilleux et al. 2009; Nardini et al. 2010; Risaliti et al. 2010).

Our results are in good agreement within the errors with those by Lee et al. (2012), who obtained the AGN-to-total luminosity ratio of 6%–8% in LIRGs and 11%–19% in ULIRGs, using a similar sample to ours that preferentially includes optically non-Seyfert infrared galaxies. They calculated the AGN contribution by performing an SED fit with the DECOMPIR package (Mullaney et al. 2011). This method requires infrared SED data covering the far-infrared band, while our method only uses the *AKARI* 2.5–5 μm spectra. This supports that our simple assumption in the spectral model (i.e., single blackbody for dust emission) works well in estimating the AGN luminosity. This simple method will have a great advantage in the era of *JWST*, because we can apply our method to high- z galaxies by observing the rest 2.5–5.0 μm band (5.0–10.0 μm at $z = 1$ and 7.5–15.0 μm at $z = 2$) with *JWST*/MIRI (5–28 μm). Other methods based on the *Spitzer* bandpass (5–35 μm) would have difficulty studying high- z objects; for instance, the observed spectral range corresponds to 15–105 μm at $z = 2$, which only the *SPICA* mission can cover. Thus, our method is achievable for studying infrared galaxies in the distant universe even before the launch of *SPICA* (from 2025–).

Combining our result with the total infrared luminosity density produced by U/LIRGs in the local universe ($\Omega_{\text{IR}}^{(\text{LIRG})} \sim 5.9 \times 10^6 L_{\odot} \text{Mpc}^{-3}$ and $\Omega_{\text{IR}}^{(\text{ULIRG})} \sim 1.4 \times 10^5 L_{\odot} \text{Mpc}^{-3}$; Goto et al. 2011), we estimate the local AGN luminosity density in the

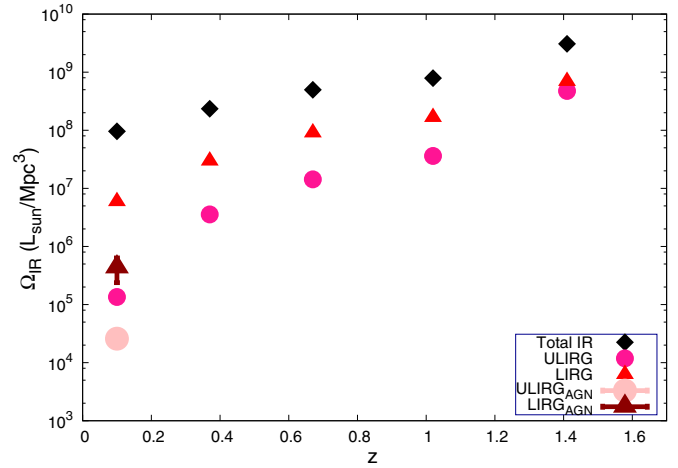


Figure 7. Comoving infrared luminosity density as a function of redshift. Black filled diamonds represent the infrared luminosity density (Ω_{IR}) of all galaxies, pink filled circles that of ULIRGs ($\Omega_{\text{IR}}^{(\text{ULIRG})}$), and red filled triangles that of LIRGs ($\Omega_{\text{IR}}^{(\text{LIRG})}$), taken from Goto et al. (2010, 2011). Pale pink filled circles and brown filled triangles represent the AGN infrared luminosity density of ULIRGs and of LIRGs, respectively, estimated by our work.

(A color version of this figure is available in the online journal.)

infrared band ($\Omega_{\text{IR}}^{(\text{AGN})}$). We find $\Omega_{\text{IR}}^{(\text{AGN})} = 4.4 \times 10^5 L_{\odot} \text{Mpc}^{-3}$ for LIRGs and $\Omega_{\text{IR}}^{(\text{AGN})} = 2.6 \times 10^4 L_{\odot} \text{Mpc}^{-3}$ for ULIRGs. These values are about an order of magnitude lower than the estimate by Goto et al. (2011). This is because Goto et al. (2011) simply assumed that the infrared luminosity of galaxies classified as AGNs entirely originates from AGNs, while we quantitatively take into account the fraction of AGN contribution to the total infrared luminosity of infrared galaxies. Figure 7 shows the infrared luminosity density as a function of redshift derived by Goto et al. (2010, 2011) together with our results for AGN infrared luminosity density. In the era of *JWST*, we can fill in the AGN infrared luminosity density at high redshifts thanks to their improved sensitivity in the mid-infrared band.

5.4. Evolutionary Track of IR Galaxies

Comparison between the SB and AGN activity gives crucial information to understand the process of galaxy–SMBH coevolution. For optically selected Seyfert galaxies and QSOs, many authors found that the luminosity of star formation (L_{SF}) and that of AGNs ($L_{\text{bol}}^{(\text{AGN})}$) are well correlated with each other (Netzer 2009; Oi et al. 2010; Imanishi et al. 2011a). We can derive an SF luminosity as $L_{\text{SF}} = L_{\text{IR}} - L_{\text{BB}}^{(\text{dust})}$. The AGN-heated dust luminosity ($L_{\text{BB}}^{(\text{dust})}$) summarized in Table 3 can be converted to an AGN bolometric luminosity ($L_{\text{bol}}^{(\text{AGN})}$) by using two relations given in Gandhi et al. (2009) and Marchese et al. (2012), respectively,

$$\log L_{2-10\text{keV}} = 0.90 \log L_{\text{MIR}}^{(\text{AGN})} + 4.09 \quad (8)$$

$$\log L_{\text{bol}}^{(\text{AGN})} \sim \log L_{\text{disk}} = 1.18 \log L_{2-10\text{keV}} - 6.68. \quad (9)$$

Here L_{disk} represents the intrinsic luminosity of the accretion disk integrated in the optical to X-ray band. Assuming $L_{\text{MIR}}^{(\text{AGN})} \sim L_{\text{BB}}^{(\text{dust})}$, we obtain

$$\log L_{\text{bol}}^{(\text{AGN})} \sim 1.06 \log L_{\text{BB}}^{(\text{dust})} - 1.85. \quad (10)$$

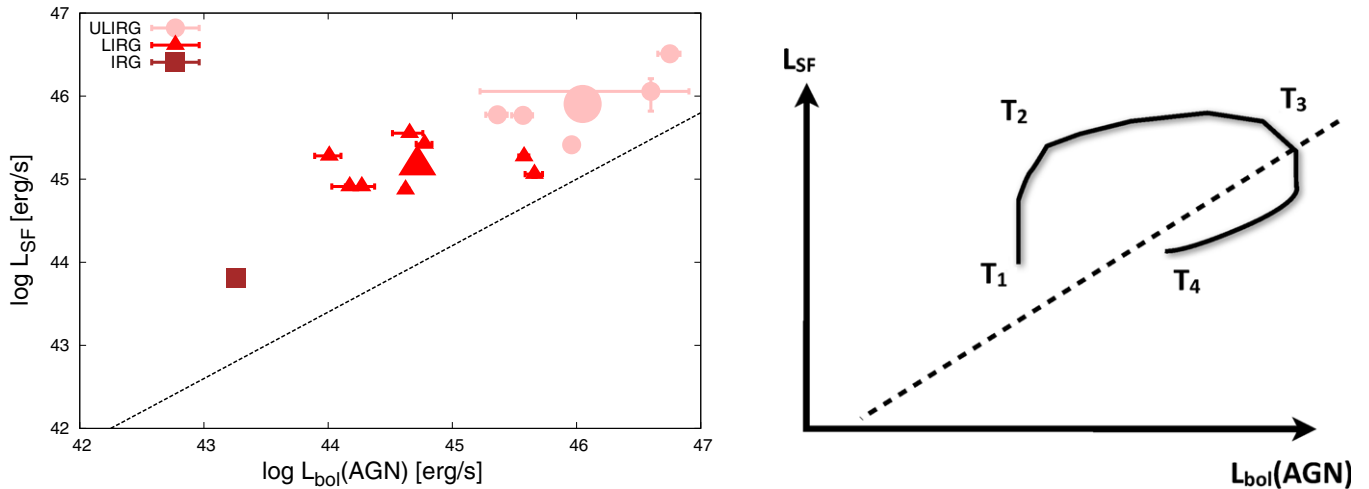


Figure 8. Left: plot of SF luminosity (L_{SF}) vs. AGN bolometric luminosity ($L_{\text{bol}}^{\text{(AGN)}}$). The dotted line represents the correlation line for optically selected Seyfert galaxies taken from Netzer (2009). All symbols and colors are the same as Figure 3. Right: schematic illustrating a scenario of AGN evolution from a pure SB galaxy to an unburied AGN phase. T_1 represents the evolutionary stage when SB is triggered by merger, T_2 when AGN activity is induced by a strong SB, T_3 when SB activity starts to decrease owing to the shortage of gas and feedback from the AGN, and T_4 when both SB and AGN activities become weaker.

(A color version of this figure is available in the online journal.)

Note that the estimated bolometric AGN luminosity ($L_{\text{bol}}^{\text{(AGN)}}$) derived in Equation (10) can be overestimated. The relations from Equations (8)–(10) are derived from the sample of nonhidden Seyfert AGNs, while our sources are infrared galaxies with highly obscured (=hidden) AGNs. Therefore, our sources in this study could have higher covering fraction of dusty torus than those of Seyfert AGNs. This means that the ratio of mid-infrared over bolometric luminosity in our sources could be larger than those of Seyfert AGNs.

Figure 8 shows the L_{SF} versus $L_{\text{bol}}^{\text{(AGN)}}$ relations obtained from our sample. The average luminosities of U/LIRG are also plotted in the same figure. The dotted line corresponds to the linear correlation obtained from optically selected Seyfert galaxies obtained by Netzer (2009). Interestingly, all the sources except two (IRAS F07353+2903 and ESO 286–IG19) are located above the Seyfert line. This result may reflect the difference in the evolutionary stage of galaxies, from a pure SB phase (U/LIRGs) to an unburied AGN phase (Seyferts). As discussed in Section 5.2, U/LIRGs have recently experienced or are facing mergers, which result in strong SB activity from the epoch T_1 to T_2 in Figure 8. The SB also triggers AGN activity, which continues from T_2 to T_3 . Finally, the SB activity is gradually weakened due to the shortage of gas and feedback from the AGN, and the supply of matter from the host galaxy onto the central engine also decreases, from T_3 to T_4 . In this framework of galaxy evolution, the evolutionary stage of ULIRGs should be a later phase of mergers than that of LIRGs. The picture is in good agreement with observations that the morphology of ULIRGs is more compact than that of LIRGs, suggesting that ULIRGs have just finished the merger process while that of LIRGs is still ongoing. This scenario suggests that infrared galaxies containing buried AGNs could be an earlier evolutionary stage of AGNs, which will be evolved to normal (unburied) Seyferts/QSOs. This scenario becomes much more reasonable if our bolometric AGN luminosity ($L_{\text{bol}}^{\text{(AGN)}}$) is overestimated as discussed in the previous paragraph because all the points are shifted to the left in the figure. While our sample size is still small, the new AGN diagnostics developed in this paper can be applied to other sources. Further studies using a

well-defined complete sample of infrared galaxies should be urged to complete our view of AGN evolution.

6. CONCLUSIONS

We obtained the *AKARI* 2.5–5.0 μm spectra of 22 infrared galaxies at $z < 0.35$ selected mainly from three infrared catalogs: bright ULIRG catalog (Klaas et al. 2001), *IRAS* 12 μm galaxy catalog (Spinoglio et al. 2002), and *IRAS* bright galaxy catalog (Soifer et al. 1987; Carico et al. 1988). This band includes unique spectral features for finding “buried” AGNs, the 3.3 μm PAH emission line and red continuum spectra originated from AGN torus emission. We perform detailed spectral fitting to these data by properly modeling the continuum and emission/absorption features. This enables us to decompose the continuum spectra into SB and AGN torus-dust components. The results are summarized as follows.

1. Using the AGN diagnostics based on the torus-dust continuum ($T^{\text{(dust)}} > 200 \text{ K}$ or $L_{\text{BB}}^{\text{(dust)}} > 10^{42} \text{ erg s}^{-1}$) and 3.3 μm PAH emission strength ($\text{EW}_{3.3\text{PAH}} < 40 \text{ nm}$), we find that 14 out of the 22 infrared galaxies have buried AGNs. We confirm the trend that the buried AGN fraction increases with infrared luminosity: $17 \pm 15\%$ for normal IRGs, $72 \pm 13\%$ for LIRGs, and $100^{+0}_{-37}\%$ for ULIRGs in our sample. This suggests that the presence of buried AGNs is ubiquitous in U/LIRGs.
2. The ratio $L_{3.3\text{PAH}}/L_{\text{IR}}$ decreases with infrared luminosity. This is opposed to the previous reports that $L_{3.3\text{PAH}}/L_{\text{IR}}$ have a constant value (Mouri et al. 1990; Imanishi 2002). This decrease is possibly due to three effects: (1) destruction of PAH molecules by X-rays emitted from the AGN, (2) PAH destruction by merger processes, and (3) increase of AGN contribution to the total infrared luminosity.
3. The energy contribution from the AGN torus-dust emission to the total infrared luminosity also increases with infrared luminosity, but it only reaches $\sim 7\%$ in LIRGs and $\sim 20\%$ even in ULIRGs. This suggests that the majority of the total infrared luminosity in U/LIRGs originates from SBs, *not* from AGNs.

4. Combining the above results with the luminosity function of infrared galaxies derived by Goto et al. (2010, 2011), we estimate the AGN luminosity density of $\Omega_{\text{IR}}^{(\text{AGN})} = 4.4 \times 10^5 L_{\odot} \text{ Mpc}^{-3}$ for LIRGs and $\Omega_{\text{IR}}^{(\text{AGN})} = 2.6 \times 10^4 L_{\odot} \text{ Mpc}^{-3}$ for ULIRGs in the local universe.
5. The L_{SF} versus $L_{\text{bol}}^{(\text{AGN})}$ luminosity plot for our sample shows that infrared galaxies with buried AGNs are located above the luminosity correlation line derived from optically selected Seyfert galaxies. We interpret that infrared galaxies could be an early phase of the evolutionary track of AGNs.

We are grateful to Kenichi Yano and Rika Yamada for their help with the data reduction of *AKARI*. We also thank Claudio Ricci and Kenta Matsuoka for discussions. The research is based on observations with *AKARI*, a JAXA project with the participation of ESA. This work was partly supported by the Grant-in-Aid for JSPS Fellows for young researchers (K.I.) and for Scientific Research 23540273 (M.I.) and 26400228 (Y.U.).

REFERENCES

- Alonso-Herrero, A., Pereira-Santaella, M., Rieke, G. H., & Rigopoulou, D. 2012, *ApJ*, **744**, 2
- Alonso-Herrero, A., Ramos Almeida, C., Mason, R., et al. 2011, *ApJ*, **736**, 82
- Asensio Ramos, A., & Ramos Almeida, C. 2009, *ApJ*, **696**, 2075
- Brightman, M., & Nandra, K. 2011, *MNRAS*, **413**, 1206
- Brightman, M., & Ueda, Y. 2012, *MNRAS*, **423**, 702
- Carico, D. P., Sanders, D. B., Soifer, B. T., et al. 1988, *AJ*, **95**, 356
- Di Matteo, T., Springel, V., & Hernquist, L. 2005, *Natur*, **433**, 604
- Draine, B. T. 1989, in *ESA Symp. 290, Infrared Spectroscopy in Astronomy*, ed. B. H. Kaldeich (Noordwijk: ESA), 93
- Eguchi, S., Ueda, Y., Awaki, H., et al. 2011, *ApJ*, **729**, 31
- Eguchi, S., Ueda, Y., Terashima, Y., Mushotzky, R., & Tueller, J. 2009, *ApJ*, **696**, 1657
- Gandhi, P., Horst, H., Smette, A., et al. 2009, *A&A*, **502**, 457
- Goto, T., Arnouts, S., Inami, H., et al. 2011, *MNRAS*, **410**, 573
- Goto, T., Takagi, T., Matsuhara, H., et al. 2010, *A&A*, **514**, A6
- Goulding, A. D., Alexander, D. M., Bauer, F. E., et al. 2012, *ApJ*, **755**, 5
- Hopkins, A. M., & Beacom, J. F. 2006, *ApJ*, **651**, 142
- Hopkins, P. F., Hernquist, L., Cox, T. J., et al. 2006, *ApJS*, **163**, 1
- Hunt, L. K., Giovanardi, C., & Helou, G. 2002, *A&A*, **394**, 873
- Ichikawa, K., Ueda, Y., Terashima, Y., et al. 2012a, *ApJ*, **754**, 45
- Ichikawa, K., Ueda, Y., Terashima, Y., et al. 2012b, *Torus Workshop*, **2012**, 109
- Iked, S., Awaki, H., & Terashima, Y. 2009, *ApJ*, **692**, 608
- Imanishi, M. 2002, *ApJ*, **569**, 44
- Imanishi, M., & Dudley, C. C. 2000, *ApJ*, **545**, 701
- Imanishi, M., Dudley, C. C., & Maloney, P. R. 2006, *ApJ*, **637**, 114
- Imanishi, M., Ichikawa, K., Takeuchi, T., et al. 2011, *PASJ*, **63**, 447
- Imanishi, M., Imase, K., Oi, N., & Ichikawa, K. 2011, *AJ*, **141**, 156
- Imanishi, M., & Maloney, P. R. 2003, *ApJ*, **588**, 165
- Imanishi, M., Nakagawa, T., Ohya, Y., et al. 2008, *PASJ*, **60**, 489
- Imanishi, M., Nakagawa, T., Shirahata, M., Ohya, Y., & Onaka, T. 2010, *ApJ*, **721**, 1233
- Kishimoto, M., Hönig, S. F., Antonucci, R., et al. 2011, *A&A*, **536**, A78
- Klaas, U., Haas, M., Müller, S. A. H., et al. 2001, *A&A*, **379**, 823
- Krolik, J. H., & Begelman, M. C. 1986, *ApJL*, **308**, L55
- Lee, J. C., Hwang, H. S., Lee, M. G., Kim, M., & Lee, J. H. 2012, *ApJ*, **756**, 95
- Le Floch, E., Papovich, C., Dole, H., et al. 2005, *ApJ*, **632**, 169
- Lira, P., Videla, L., Wu, Y., et al. 2013, *ApJ*, **764**, 159
- Lu, N., Helou, G., Werner, M. W., et al. 2003, *ApJ*, **588**, 199
- Lutz, D., Feuchtgruber, H., Genzel, R., et al. 1996, *A&A*, **315**, L269
- Magnelli, B., Elbaz, D., Chary, R. R., et al. 2011, *A&A*, **528**, A35
- Maiolino, R., Comastri, A., Gilli, R., et al. 2003, *MNRAS*, **344**, L59
- Marchese, E., Della Ceca, R., Caccianiga, A., et al. 2012, *A&A*, **539**, A48
- Mihos, J. C., & Hernquist, L. 1996, *ApJ*, **464**, 641
- Moorwood, A. F. M. 1986, *A&A*, **166**, 4
- Mouri, H., Kawara, K., Taniguchi, Y., & Nishida, M. 1990, *ApJL*, **356**, L39
- Mullaney, J. R., Alexander, D. M., Goulding, A. D., & Hickox, R. C. 2011, *MNRAS*, **414**, 1082
- Murakami, H., Baba, H., Barthel, P., et al. 2007, *PASJ*, **59**, 369
- Murphy, E. J., Chary, R.-R., Dickinson, M., et al. 2011, *ApJ*, **732**, 126
- Nardini, E., Risaliti, G., Salvati, M., et al. 2008, *MNRAS*, **385**, L130
- Nardini, E., Risaliti, G., Salvati, M., et al. 2009, *MNRAS*, **399**, 1373
- Nardini, E., Risaliti, G., Watabe, Y., Salvati, M., & Sani, E. 2010, *MNRAS*, **405**, 2505
- Neenkova, M., Sirocky, M. M., Ivezić, Ž., & Elitzur, M. 2008a, *ApJ*, **685**, 147
- Neenkova, M., Sirocky, M. M., Nikutta, R., Ivezić, Ž., & Elitzur, M. 2008b, *ApJ*, **685**, 160
- Netzer, H. 2009, *MNRAS*, **399**, 1907
- Nishiyama, S., Tamura, M., Hatano, H., et al. 2009, *ApJ*, **696**, 1407
- Ohyama, Y., Onaka, T., Matsuhara, H., et al. 2007, *PASJ*, **59**, 411
- Oi, N., Imanishi, M., & Imase, K. 2010, *PASJ*, **62**, 1509
- Onaka, T., Matsuhara, H., Wada, T., et al. 2007, *PASJ*, **59**, 401
- Oyabu, S., Ishihara, D., Malkan, M., et al. 2011, *A&A*, **529**, A122
- Petric, A. O., Armus, L., Howell, J., et al. 2011, *ApJ*, **730**, 28
- Ramos Almeida, C., Levenson, N. A., Alonso-Herrero, A., et al. 2011, *ApJ*, **731**, 92
- Ramos Almeida, C., Levenson, N. A., Rodríguez Espinosa, J. M., et al. 2009, *ApJ*, **702**, 1127
- Ricci, C., Walter, R., Courvoisier, T. J.-L., & Paltani, S. 2011, *A&A*, **532**, 102
- Risaliti, G., Imanishi, M., & Sani, E. 2010, *MNRAS*, **401**, 197
- Risaliti, G., Maiolino, R., Marconi, A., et al. 2006, *MNRAS*, **365**, 303
- Rush, B., Malkan, M. A., & Spinoglio, L. 1993, *ApJS*, **89**, 1
- Sanders, D., & Ishida, C. 2004, in *ASP Conf. Ser. 320, The Neutral ISM in Starburst Galaxies*, ed. S. Aalto, S. Huttemeister, & A. Pedlar (San Francisco, CA: ASP), 230
- Sanders, D. B., & Mirabel, I. F. 1996, *ARA&A*, **34**, 749
- Sanders, D. B., Soifer, B. T., Elias, J. H., et al. 1988, *ApJ*, **325**, 74
- Sani, E., Risaliti, G., Salvati, M., et al. 2008, *ApJ*, **675**, 96
- Sawicki, M. 2002, *AJ*, **124**, 3050
- Siebmorgen, R. 1993, *ApJ*, **408**, 218
- Soifer, B. T., Neugebauer, G., Matthews, K., et al. 2001, *AJ*, **122**, 1213
- Soifer, B. T., Sanders, D. B., Madore, B. F., et al. 1987, *ApJ*, **320**, 238
- Spinoglio, L., Andreani, P., & Malkan, M. A. 2002, *ApJ*, **572**, 105
- Spinoglio, L., Malkan, M. A., Rush, B., Carrasco, L., & Recillas-Cruz, E. 1995, *ApJ*, **453**, 616
- Stalevski, M., Fritz, J., Baes, M., Nakos, T., & Popović, L. Č. 2012, *MNRAS*, **420**, 2756
- Ueda, Y., Eguchi, S., Terashima, Y., et al. 2007, *ApJL*, **664**, L79
- Veilleux, S., Kim, D.-C., & Sanders, D. B. 1999, *ApJ*, **522**, 113
- Veilleux, S., Kim, D.-C., & Sanders, D. B. 2002, *ApJS*, **143**, 315
- Veilleux, S., Kim, D.-C., Sanders, D. B., Mazzarella, J. M., & Soifer, B. T. 1995, *ApJS*, **98**, 171
- Veilleux, S., Rupke, D. S. N., Kim, D.-C., et al. 2009, *ApJS*, **182**, 628
- Videla, L., Lira, P., Andrews, H., et al. 2013, *ApJS*, **204**, 23
- Winter, L. M., Mushotzky, R. F., Reynolds, C. S., & Tueller, J. 2009, *ApJ*, **690**, 1322
- Yamada, R., Oyabu, S., Kaneda, H., et al. 2013, *PASJ*, **65**, 103
- Yuan, T.-T., Kewley, L. J., & Sanders, D. B. 2010, *ApJ*, **709**, 884